Award Number: W81XWH-10-1-0714

TITLE: Magnetic Resonance Characterization of Axonal Response to Spinal Cord Injury

PRINCIPAL INVESTIGATOR: Felix W. Wehrli, Ph.D.

CONTRACTING ORGANIZATION: University of Pennsylvania
Philadelphia, PA 19104

REPORT DATE: June 2015

TYPE OF REPORT: Final

PREPARED FOR: U.S. Army Medical Research and Materiel Command
Fort Detrick, Maryland 21702-5012

REPORT DOCUMENTATION PAGE

Form Approved
OMB No. 0704-0188

1. REPORT DATE *(DD-MM-YYYY)*	**2. REPORT TYPE**	**3. DATES COVERED** *(From - To)*
June 2015	Final	09/27/2010 – 03/26/2015

4. TITLE AND SUBTITLE

Magnetic Resonance Characterization of Axonal Response to Spinal Cord Injury

5a. CONTRACT NUMBER

5b. GRANT NUMBER
W81XWH-10-1-0714

5c. PROGRAM ELEMENT NUMBER

6. AUTHOR(S)

Felix W. Wehrli, Ph.D.

email: wehrli@mail.med.upenn.edu

5d. PROJECT NUMBER

5e. TASK NUMBER

5f. WORK UNIT NUMBER

7. PERFORMING ORGANIZATION NAME(S) AND ADDRESS(ES)

University of Pennsylvania
Office of Research Services
3451 Walnut Street, Room P-221
Philadelphia PA 19104-6205

8. PERFORMING ORGANIZATION REPORT NUMBER

9. SPONSORING / MONITORING AGENCY NAME(S) AND ADDRESS(ES)

U.S Army Medical Research and Material Command
Fort Detrick, MD 21702-5012

10. SPONSOR/MONITOR'S ACRONYM(S)

11. SPONSOR/MONITOR'S REPORT NUMBER(S)

12. DISTRIBUTION / AVAILABILITY STATEMENT

Approved for public release; distribution unlimited

13. SUPPLEMENTARY NOTES

14. ABSTRACT

Assessment of axon health in spinal cord injury (SCI) is vital for proper diagnosis and treatment. Magnetic resonance imaging (MRI) is routinely performed in patients and provides valuable information about cord edema and hemorrhage. However, comprehensive prediction of axonal changes from in vivo MR imaging remains elusive. At the U. Penn site, we are applying two novel MRI methods to the problem of assessment of axonal loss, axonal diameter distribution, and myelin loss (q-space imaging (QSI) and ultra-short echo-time (UTE) MRI) first on animal specimens and then on human subjects.

During the final period of the project the focus of the research was on the core aim, which was to study Wallerian degeneration of spinal cord axons in a mouse injury model. Injury was induced by hemisection of the spinal cord (i.e. sectioning of only one hemisphere of the spinal cord, leaving the contralateral side intact, thereby providing an internal control). Spinal cords were examined after perfusion fixation by means of a quantitative magnetic resonance technique, called Q=space imaging or QSI, that provides indirect information on axonal structure by measuring diffusion of tissue water perpendicular to the spinal cord axis. Spinal cords were studied 3 weeks and 3 months post injury. Spinal cord degeneration was clearly evident and quantifiable at locations distant to the injury site in conformance with hypothesis. Finally, histologic images were obtained, which allow for direct visualization of axons. This portion of the project could not be completed yet but it is planned to finish the project provided funds can be obtained from other sources.

15. SUBJECT TERMS

Axon Architecture, Spinal Cord Injury, Axon Loss, Myelin, Q-Space Imaging, UTE, MRI

16. SECURITY CLASSIFICATION OF:			**17. LIMITATION OF ABSTRACT**	**18. NUMBER OF PAGES**	**19a. NAME OF RESPONSIBLE PERSON**
					USAMRMC
a. REPORT	**b. ABSTRACT**	**c. THIS PAGE**	UU	17	**19b. TELEPHONE NUMBER** *(include area code)*
U	U	U			

Table of Contents

DOD Award W81XWH-10-1-0714
Final Report
September 2010 - March 2015

University of Pennsylvania Site: PI Felix W Wehrli

Executive Summary

The overarching objective of this project was to address the hypothesis that, in an animal model of spinal cord injury, Q-space magnetic resonance imaging (QSI) is able to identify and quantify the extent of axonal damage from Wallerian degeneration (WD). QSI is a MRI technique that is sensitive to diffusion of tissue water molecules at the cellular level. While free diffusion is Gaussian, diffusion restricted by barriers imposed by cell membranes, is not. Hence, disintegration of the axonal architecture upon injury causes a measurable effect on the water diffusion behavior, including a broadening of the displacement profile, representative of myelin loss and increased permeability of axon membrane. The loss of myelin, another hallmark of WD, can be assessed by direct or indirect imaging of myelin, an associated Aim of the project. Toward the project's key objectives a mouse spinal cord injury (SCI) model involving spinal cord hemisection was investigated. In brief, sixteen mouse spinal cords, provided by the Drexel University partnering organization, were studied *ex vivo* with imaging techniques developed at the U. Penn site. Four were control specimens, and the remaining 12 were derived from mice undergoing a dorsal-lateral funiculotomy at the C-6 level. Six spinal cords were harvested three weeks after injury and six cords were harvested three months after injury. Spinal cords were perfusion fixed and underwent QSI at 400 MHz with a protocol similar to that described in our prior work to yield diffusion displacement profiles, which provide quantitative information on axonal structure indirectly, thus having potential for translation to humans with SCI. The plan then was to compare the QSI data with histology as ground truth. The QSI data yielded significant new insight. The three parameters characterizing the displacement profile showed a strong response at the ipsilateral site of injury, extending over a significant distance in both rostral and caudal direction (see sections below for detail). Unfortunately, the goal to compare the QSI data with histology was not attained. However, the projected yielded other related new data. Since myelination is at the core of WD, a nondestructive method for quantifying myelin density would have major impact. Here, we showed, for the first time, that direct imaging of myelin by quantitative MRI is possible (Wilhelm et al, PNAS 2012). Importantly, this DOD funded research provided the basis for a grant from NIH (R21-NS082953, "Feasibility of Direct Quantitative Magnetic Resonance Imaging of Myelin", PI FW Wehrli). We further showed that the QSI method may be applicable on clinical scanners by providing data in the excised pig spinal cord (similar in dimension to the human spinal cord). Our data suggest that different tracts (known from histology to differ in axon diameter) could be correctly sized on the basis of the QSI displacement profiles, thereby laying the groundwork for future studies in humans. – We had many odds against us in this project, starting with the change-over of the micro-MRI instrumentation, which necessitated re-implemention of the pulse sequences after many months of down-time. Subsequently, our custom-made gradient insert failed, fatally as it turned out, which after numerous attempts to repair the hardware, led us to adapt the protocol to the manufacturer's far less powerful standard imaging gradients. Lastly, the Drexel researchers who were assigned to perform the histologic analyses, were out of funding and personnel, which required us to find a new lab able and equipped to do both sectioning and generation of the digital images.

Methods and Results

Q-Space Imaging and Analysis

Q-space imaging (QSI) was performed on a total of 16 fixed mouse spinal cords. Spinal cords were first trimmed to remove the brain stem (to ensure that the specimen fit into a 5 mm NMR tube) and cut at the mid-thoracic level. A custom holder was constructed to hold a spinal cord inside a 5 mm NMR tube, which was then filled with Fomblin. Based on a spin-echo T2-weighted image, the site of injury could be identified as a dark line. A 13-slice, 2D QSI experiment was performed on each spinal cord with the site of injury centered in slice

6. QSI processing was performed using a custom Matlab program to produce three parametric maps for each slice: full-width-at-half-maximum (FWHM), zero-displacement probability (ZDP), and kurtosis described in our earlier work.

ROIs were manually drawn as shown in **Figure 1**. The spinal cord was divided into left and right halves and each halve was subdivided into six ROIs for a total of 12 ROIs. With 13 MRI slices and 12 ROIs for each slice, a total of 156 ROIs were manually drawn and analyzed. For each ROI, mean and standard deviation was recorded for all FWHM, ZDP, and kurtosis maps resulting from pixelwise analysis of the QSI displacement profiles (FWHM=full width at half maximum, ZDP=zero displacement probability, kurtosis=deviation of gaussianity). The unique aspect of this dataset is the ability to assess axonal injury at several distances both rostral and caudal from the site of injury as well as at different time points, and to do so for individual tracts (details not shown). As injury is only induced on the right side (ipsilateral), the left side of the spinal cord can be used as a contralateral control. **Figure 2** shows three-week and three-month FWHM, ZDP, and kurtosis values from the lateral dorsal ROI for each MRI slice. The values are averaged over all specimens.

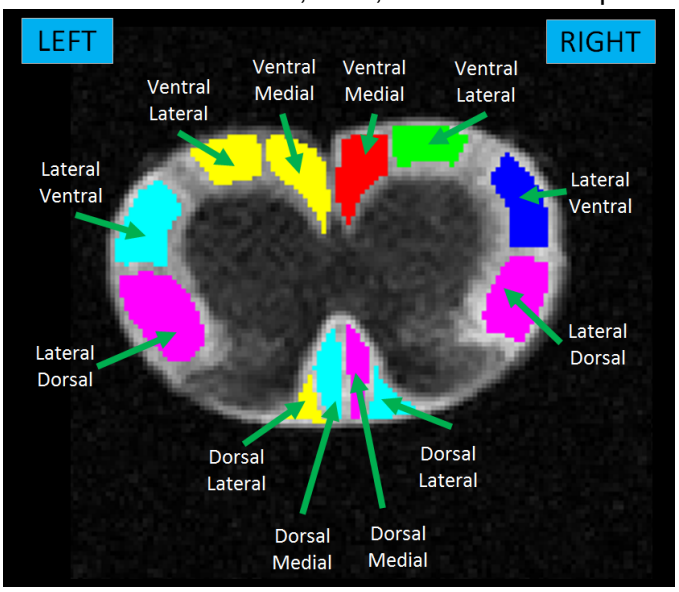

Figure 1. Representative manual ROIs overlaid on an axial diffusion-weighted image.

As hypothesized, the injured ROI values showed consistently higher FWHM, and lower ZDP and kurtosis values compared with control ROI values, suggesting degradation in axon morphology. Slice 6 shows the greatest loss of axon integrity based on QSI metrics, which is expected as the site of injury was centered on slice 6.

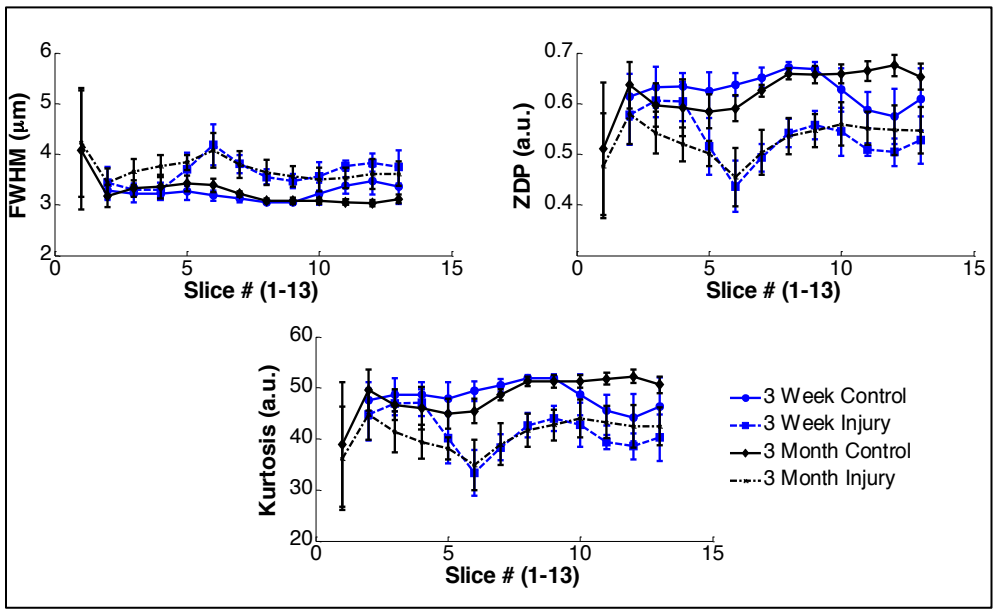

Figure 2. Mean and standard deviation of FWHM, ZDP, and kurtosis values from lateral dorsal ROI averaged over all specimens for each MRI slice position. Three-week values are shown in blue and 3-month values in black. Contralateral control ROI values are displayed with solid lines, while injured ROI values are displayed with dashed lines. Slices are numbered in the rostral-caudal direction.

Histology

All mouse spinal cords were embedded in resin prior to sectioning with a microtome. The embedded block portion is located from 2mm to 6mm from the rostral end of the cord. As determined on the basis of the MRI images, injuries are located approximately 4mm from the rostral end, placing them at the center of the resin blocks. Sections 1 micron thick were collected at roughly 250, 500, 1000, 1250, 1500, 1750, 2000, 2250, 2500, 2750, 3000, 3500 μm from the rostral end of the block (yielding on average 11 to 12 sections per sample). Each slide was then then coverslipped with Permount and a thin plate of glass before being digitized. This work, unfortunately, could not be completed due to exhaustion of funds and departure of one of the investigators but it is hoped that supplementary funding can be obtained in the future to complete the work.

We have conceived and implemented a semi-automated method for segmenting the axons on the basis of the histological images. Although the contrast is adequate between intra- and extra-axonal regions the main difficulty is the heterogeneity of the staining. Thus, using a simple threshold for the segmentation fails. We therefore conceived and implemented a semi-automated segmentation algorithm where the user drags a small ellipsoidal region across the image in a manner such that the staining intensity is roughly linear within the ellipse. As the user holds down and drags the mouse button, the software does the linear correction in real time and shows the segmentation in real time. Using keyboard arrows, the size and shape of the ellipse may be modified as well as the threshold level (which is applied after the linear correction). In this way the segmentation may be performed rapidly while avoiding situations where the ellipsoidal region contains a nonlinear staining gradient (**Figure 3**).

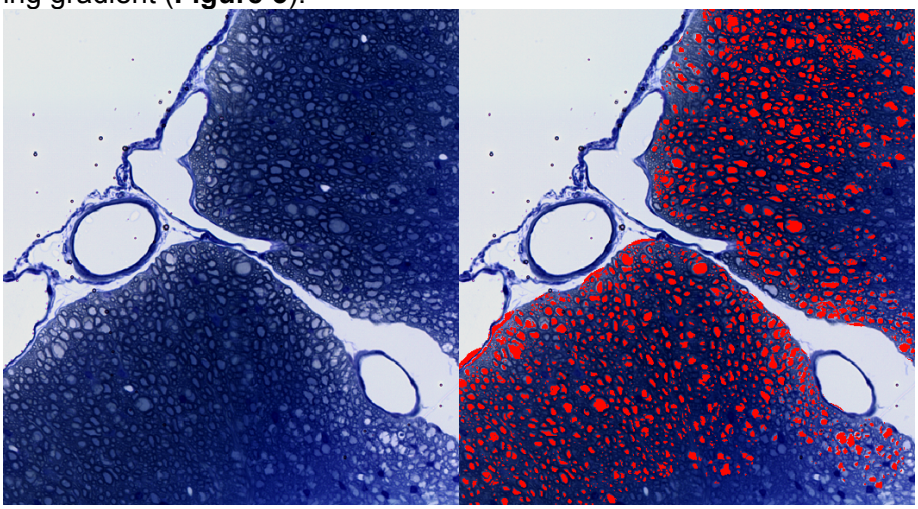

a b

Figure 3. A section of the histological image before (a) and after segmentation (b). Segmentation was performed with the semi-automated algorithm described above where the user drags a small ellipsoidal area across the regions of interest (ROI) in a manner that avoids locally nonlinear staining gradients.

QSI Feasibility on Clinical Scanners

Progress has been made toward translation of the QSI methodology to the clinic (in support of Aim 3 pursued at the Harvard site). QSI displacement maps obtained at 1.5T on a clinical imager on fixed pig spinal cords yielded the characteristic axon diameters for dorsal, lateral and ventral tracts. Since the pig spinal cord is similar in size to the human spinal cord and the experiments were performed with standard imaging gradients the results suggest feasibility of performing studies in humans with spinal cord injury (even though this was not a specific objective of the current project). This research was presented at the 2012 Annual Meeting of the International Society for Magnetic Resonance in Medicine in Melbourne, Australia. **Figures 4a** and **b** show analyzed white matter regions and mean displacements in the three regions, commensurate with the different axon sizes.

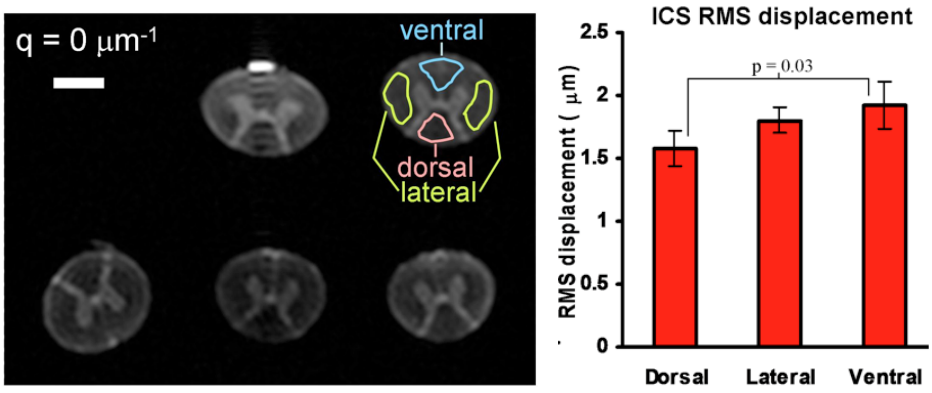

Figure 4 a) Sample transverse images of pig spinal cord acquired at 1.5T with regions of interest indicated (white bar = 5mm); b) RMS displacement obtained from QSI displacement maps consistent with known axon diameters in the three WM tracts examined.

Direct MR Imaging of Myelin

Until our present work neural myelin could only indirectly be mapped either by relaxometric detection of myelin water or magnetization transfer. Here, we investigated whether myelin can be detected and possibly quantified directly. We identified the spectrum of myelin in the spinal cord *in situ* as well as in myelin lipids extracted via a sucrose gradient method, and investigated its spectral properties. High-resolution solution nuclear magnetic resonance spectroscopy showed the extract composition to be in agreement with myelin's known chemical make-up. The 400MHz ^{1}H spectrum of the myelin extract, at 20ºC (room temperature) and 37ºC, consists of a narrow water resonance superimposed on a broad envelope shifted approximately 3.5ppm upfield, suggestive of long-chain methylene protons. Superimposed on this signal are narrow components resulting from functional groups matching the chemical shifts of the constituents making up myelin lipids. The spectrum could be modeled as a sum of super-Lorentzians with a T_2^* distribution covering a wide range of values (0.008-26ms). Overall, there was a high degree of similarity in the spectral properties of extracted myelin lipids with those found in neural tissue. The normalized difference spectrum had the hallmarks of membrane proteins, not present in the myelin extract. Using 3D radially ramp-sampled proton MRI, with a combination of adiabatic inversion and echo subtraction, the feasibility of direct myelin imaging *in situ* is demonstrated. Lastly, the integrated signal from myelin suspensions is shown, both spectroscopically and by imaging, to scale with concentration, suggesting the potential for quantitative determination of myelin density.

Key Research Accomplishments

- Demonstrated feasibility of direct imaging of neural myelin as a new metric for the evaluation of spinal cord injury.
- Isolated myelin and showed that its NMR properties match those of myelin in situ in the spinal cord.
- Published first paper demonstrating feasibility of direct quantitative MRI of myelin in the Proceedings of the National Academy of Sciences in 2012:
    - Characterized the magnetic resonance properties of myelin as a lamellar liquid crystal;
    - Demonstrated quantitative relationship between solid-state MRI signal and volume fraction of water-suspended reconstituted myelin;
    - Obtained pure myelin images of the mouse spinal cord *ex vivo*
- Showed in a mouse spinal cord injury model that Wallerian degeneration can be assessed quantitatively in terms of QSI metrics based on the analysis of the measured displacement pro-

files with the hypothesized changes over time extending rostral and caudal of the hemisection injury site.
- Developed an algorithm for axon structure analysis in histologic images of the mouse spinal cord
- Demonstrated the feasibility of translation of the q-space imaging technique from the laboratory to the clinic in a porcine model of the spinal cord on a 1.5T clinical imager, and therefore delineated a path toward quantitative myelin imaging in humans.

Reportable Outcomes

1. Wilhelm MJ, Ong HH, Wehrli SL, Tsai PH, Hackney DB, Wehrli FW. Direct magnetic resonance detection of myelin and prospects for quantitative imaging of myelin density. Proc Natl Acad Sci, USA 109(24): 9605-9610; 2012.

2. Wilhelm MJ, Ong HH, Wehrli SL, Tsai PH, Hackney DB, Wehrli FW. Prospects for quantitative imaging of myelin with dual-echo short inversion time 3D UTE MRI. 2011; Montréal, Québec, Canada. ISMRM. p. 2460.

3. Ong HH, Bhagat YA, Magland JF, Wehrli FW. Feasibility of low q-space diffusion MRI at 1.5T. 2012; Melbourne, Australia. ISMRM. p. 349.

4. Wilhelm MJ, Ong HH, Wehrli FW. Super-Lorentzian framework for investigation of T2* distribution in myelin. 2012; Melbourne, Australia. ISMRM. p. 2394.

5. NIH R21-NS082953 “Feasibility of Direct Quantitative Magnetic Resonance Imaging of Myelin”, PI: Felix W. Wehrli, Ph.D., 2013-2016

Personnel - Award #: DOD W81XWH-10-1-0714

Suliman Barhoum, Ph.D.
Cheng Li, Ph.D.
Jeremy Magland, Ph.D.
Henry Ong, Ph.D.
Felix W. Wehrli, Ph.D.
Michael Wilhelm, Ph.D.
Alexander Wright, Ph.D.

Direct magnetic resonance detection of myelin and prospects for quantitative imaging of myelin density

Michael J. Wilhelm[a,1], Henry H. Ong[a], Suzanne L. Wehrli[b], Cheng Li[a], Ping-Huei Tsai[a,2], David B. Hackney[c], and Felix W. Wehrli[a,3]

[a]Laboratory for Structural NMR Imaging, Department of Radiology, University of Pennsylvania School of Medicine, Philadelphia, PA 19104; [b]NMR Core Facility, Joseph Stokes Jr. Research Institute, Children's Hospital of Philadelphia, Philadelphia, PA 19104; and [c]Department of Radiology, Beth Israel Deaconess Medical Center, Harvard Medical School, Boston, MA 02115

Edited by Alan P. Koretsky, National Institutes of Health, Bethesda, MD, and accepted by the Editorial Board April 27, 2012 (received for review September 13, 2011)

Magnetic resonance imaging has previously demonstrated its potential for indirectly mapping myelin density, either by relaxometric detection of myelin water or magnetization transfer. Here, we investigated whether myelin can be detected and possibly quantified directly. We identified the spectrum of myelin in the spinal cord in situ as well as in myelin lipids extracted via a sucrose gradient method, and investigated its spectral properties. High-resolution solution NMR spectroscopy showed the extract composition to be in agreement with myelin's known chemical make-up. The 400-MHz ^{1}H spectrum of the myelin extract, at 20 °C (room temperature) and 37 °C, consists of a narrow water resonance superimposed on a broad envelope shifted ∼3.5 ppm upfield, suggestive of long-chain methylene protons. Superimposed on this signal are narrow components resulting from functional groups matching the chemical shifts of the constituents making up myelin lipids. The spectrum could be modeled as a sum of super-Lorentzians with a T_2* distribution covering a wide range of values (0.008–26 ms). Overall, there was a high degree of similarity between the spectral properties of extracted myelin lipids and those found in neural tissue. The normalized difference spectrum had the hallmarks of membrane proteins, not present in the myelin extract. Using 3D radially ramp-sampled proton MRI, with a combination of adiabatic inversion and echo subtraction, the feasibility of direct myelin imaging in situ is demonstrated. Last, the integrated signal from myelin suspensions is shown, both spectroscopically and by imaging, to scale with concentration, suggesting the potential for quantitative determination of myelin density.

myelin in situ | myelin NMR spectrum | super-Lorentzian fitting | ultrashort echo time

Myelin is a critical feature of nervous system white matter (WM) and accounts for 14% of the wet mass of WM (1). It is a lipid–protein bilayer that extends from the outer membrane of glial cells (i.e., oligodendrocytes in the CNS) and discretely winds around individual axonal fibers, leading to an increase in conduction velocity (1). By speeding conduction and reducing axonal energy requirements, myelin makes large and complex organisms possible. Myelin also contributes to the mechanical and functional structure of the axon. In addition, some oligodendrocytic cells and precursors can support action potentials themselves (2). Deficiencies of myelin lay at the core of numerous neurodegenerative disorders, such as multiple sclerosis and schizophrenia (1). These deficiencies may result from developmental or acquired abnormalities in oligodendrocyte function, which also leads to axonal degeneration. Assessment of myelin may reveal CNS abnormalities far beyond those associated with classic demyelinating diseases. MRI of myelin has the potential to characterize not only loss of this important component of the CNS but also to reveal axonal and supporting glial integrity and function.

A diverse assortment of experimental techniques has been applied toward the goal of observing and quantifying myelin. The common methods rely on optical microscopy of histologically stained tissue samples (3). X-ray diffraction (4) and nonlinear optical techniques (5, 6) also provide insight into myelin ultrastructure. Unfortunately, all these techniques are destructive and thus applicable only to animal studies.

More recently, myelin-specific chemical contrast markers that selectively bind to myelin have emerged. Such agents are currently under development for both MRI (7) and positron-emission tomography (8). Although these techniques are potentially promising, concerns over toxicity may pose significant hurdles to their clinical implementation.

So far, MRI has had the greatest impact toward nondestructive myelin assessment in both laboratory animals and humans. Further, MRI has the added benefit that signal contrast originates from endogenous protons and hence is not reliant upon injectable chemical probes nor limited by contrast-related temporal delays.

To date, two indirect MR techniques applicable to studies in vivo have demonstrated histologically correlated sensitivity to myelin: magnetization transfer (MT) and T_2 relaxometry. In MT, cross-relaxation between myelin protons and tissue water is exploited (9). The signal attenuation resulting from off-resonance saturation (MT ratio) has been found to scale with myelin concentration (10). T_2 relaxometry yields T_2 spectra, typically by inversion of the Carr-Purcell echo decay using an inverse Laplace transformation (11). Spectral components with T_2 values ranging from 10 to 50 ms have been assigned to motionally restricted myelin water (12, 13) and have demonstrated strong correlation with myelin-specific histologic staining (12, 14).

Although MT and T_2 relaxometry have shown promise, they both rely on indirect detection of myelin through the interaction of water with myelin. This complex interaction is affected by nonmyelin loss-related changes, which can lead to ambiguities in data interpretation. For example, MT is sensitive not only to myelin content but also to axon density (15). Therefore, even though both techniques may distinguish normal from abnormal WM, they rely on the invariance of the myelin–water interaction.

Direct detection of myelin with MR would remove some complications in the analysis from the intermediate effects of the

Author contributions: M.J.W., H.H.O., and F.W.W. designed research; M.J.W., H.H.O., and S.L.W. performed research; M.J.W., H.H.O., S.L.W., C.L., P.-H.T., and F.W.W. analyzed data; and M.J.W., H.H.O., C.L., D.B.H., and F.W.W. wrote the paper.

The authors declare no conflict of interest.

This article is a PNAS Direct Submission. A.P.K. is a guest editor invited by the Editorial Board.

Freely available online through the PNAS open access option.

[1]Present address: Department of Chemistry, Temple University, Philadelphia, PA 19122.

[2]Present address: Graduate Institute of Biomedical Electronics and Bioinformatics, National Taiwan University, Taipei 10617, Taiwan, Republic of China.

[3]To whom correspondence should be addressed. E-mail: wehrli@mail.med.upenn.edu.

This article contains supporting information online at www.pnas.org/lookup/suppl/doi:10.1073/pnas.1115107109/-/DCSupplemental.

interaction of water and myelin, and therefore may provide contrast specific to myelin concentration. However, direct detection is complicated by motional restriction of the lipid chains in the myelin bilayer, resulting in broad lines and, consequently, short lifetime of the MR signal.

Perhaps the first characterization of the NMR spectral properties of myelin was by Lecar et al. (16), who studied anhydrous preparations by wide-line proton spectroscopy, concluding that under these conditions the system is in a liquid–crystalline state. To the best of our knowledge, the first report of myelin proton transverse relaxation was by Ramani et al. (17). The authors performed a multiexponential fit of spin-echo decays on fixed human WM samples from normal and multiple sclerosis patients and reported a T_2 value of ~50 μs for myelin protons. They were also able to detect lipid signals by magic-angle spinning proton NMR in slices of normal WM tissue but not in multiple sclerosis lesions. Recently, Horch et al. (18) investigated the T_2^* and T_2 relaxation characteristics of myelin and reported values of ~70 μs as well as a broader distribution ranging from 50 to 1,000 μs.

The transverse relaxation properties of myelin suggest the need for ultrashort echo time (UTE) MRI methods, which entail collection of the free-induction decay immediately after excitation. Typical implementations include either 3D radial sampling with nonselective rf pulses (19) or 2D radial sampling with slice-selective half rf pulses and ramp sampling (20) as previously applied for the characterization of cortical bone matrix and bone water (21, 22).

UTE MRI has been used to image the short T_2^* (i.e., <1 ms) signal from human brain in vivo (23). Unlike applications to study bone, these implementations include long T_2^* suppression methods to attenuate the tissue water signal. Tissue water, because of its rotational mobility and high concentration, has an intense long T_2^* signal that, without suppression, overwhelms signal from short T_2^* components (Fig. S1*A*). Although the images indicated the short T_2^* signal to be predominantly located in WM, no evidence was provided to link this signal to myelin.

In this work we examine the origin and nature of the short T_2^* signal of CNS tissue in freshly excised rat spinal cord (SC) in comparison with purified myelin lipid extract with multinuclear NMR. We further explore the potential for direct detection and quantification of myelin by UTE MRI and discuss the possibilities and technical hurdles associated with translating MRI-based quantification of myelin to the clinic.

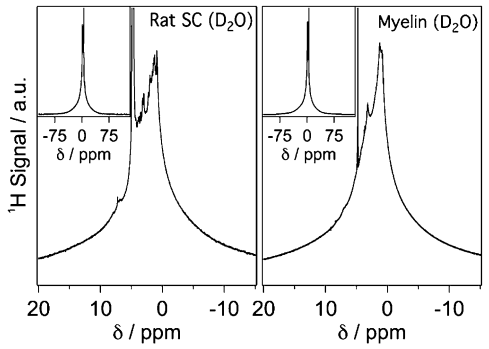

Fig. 1. The ^{1}H NMR spectra from rat thoracic SC after D_2O exchange of tissue water (*Left*) and myelin lipid extract suspended in D_2O (*Right*), showing remarkable similarity. *Insets*: Wide tails present in both spectra. Note that in addition to narrow resonances, likely stemming from proteins, the residual monodeuterium oxide (HDO) resonance is stronger in the tissue spectrum.

Results

High-Resolution ^{1}H NMR Spectra of Intact SC Tissue and Bovine Myelin Extract. Fig. 1 shows a comparison of the ^{1}H NMR spectra collected for a section of excised rat thoracic SC and a deuterium oxide (D_2O) suspension of myelin lipid extract. The SC was first immersed in 99.9% D_2O for 24 h to exchange tissue water with D_2O, and hence attenuate the bulk proton signal (Fig. S1*B*). The protein-free myelin lipid sample was chemically extracted from an intact isolated myelin sample, obtained via a sucrose gradient method (*SI Materials and Methods*) and quantitatively validated with proton-decoupled ^{13}C and ^{31}P NMR spectroscopy (Table 1 and Fig. S2 *A* and *B*).

Both ^{1}H spectra in Fig. 1 show a broad resonance with a superimposed narrow water resonance originating from residual HDO. Although the two broad resonances bear a high degree of similarity, a difference spectrum (i.e., tissue − extract) (Fig. S3) highlights the distinguishing features. First, the superimposed fine structure apparent in the SC spectrum is consistent with mobile proteins as they might occur in the cytoplasm, for example. Second, the difference spectrum contains a broad resonance as it might be expected from membrane proteins. The difference spectrum was generated such that the integrated signal area is 27.9% of the total spectrum, as expected according to the known protein fraction in myelin (details in *SI Results*). Small errors in the difference spectrum could arise because we are ignoring cytoplasmic proteins in this fraction.

UTE MRI of Intact SC. Fig. 2 shows a set of images of freshly excised rat SC, obtained with a 3D radial, ramp-sampled, dual-echo inversion recovery UTE (de-IR-UTE) pulse sequence (Fig. S4). Long T_2^* tissue water signal was attenuated via adiabatic inversion and complex echo subtraction. Adiabatic inversion was used to significantly reduce the signal intensity from tissue water, which would then be further attenuated with echo subtraction. We empirically selected TI to achieve the greatest WM intensity while minimizing gray matter (GM) intensity signal in the complex echo difference image in accordance with the expectation of low signal in GM considering its very low myelin content. Images were collected at both short (20 μs; Fig. 2*A*) and long (1,200 μs; Fig. 2*B*) TE. The magnitude of the complex difference image and signal profile (Fig. 2 *C* and *D*)

Table 1. Lipids of myelin with abbreviations used in the text

Myelin lipid	ID	Molar % Norton*	Molar % NMR†	% labile ^{1}H ± σ‡
Cholesterol	CHOL	44.8	43.1	0.94 ± 0.04
Galactocerebroside	GC	17.5	19.6	2.20 ± 0.39
Galactosulfatide	GS	2.5	NA§	0.28 ± 0.05¶
Phosphatidylethanolamine	PE	3.4	3.9	0.24 ± 0.05
PE plasmalogen	PEpl	11.3	11.8	0.70 ± 0.13
Phosphatidylcholine	PC	8.0	7.8	0.00 ± 0.00
PC plasmalogen	PCpl	0.3	2.0	0.00 ± 0.00
Sphingomyelin	Sph	5.2	5.9	0.37 ± 0.08
Phosphatidylinositol	PI	0.7	2.0	0.19 ± 0.03
Phosphatidylserine	PS	0.2	3.9	0.11 ± 0.01
Total				5.05 ± 0.79

Comparison of average bovine myelin lipid molar ratios reported by Norton et al. (25) and quantitative multi-NMR methods. Also shown are average percentages of labile protons pertaining to each lipid component. PC, phosphatidylcholine; PE, phosphatidylethanolamine.
*From Norton et al. (23).
†Present study, ^{13}C and ^{31}P NMR.
‡Variability (σ, SD) due to lipid chain length [$CH_3(CH_2)_n$; n = 10–25].
§Not measured owing to a lack of an unambiguous resonance.
¶Assuming a GS molar percentage of 2.5%.

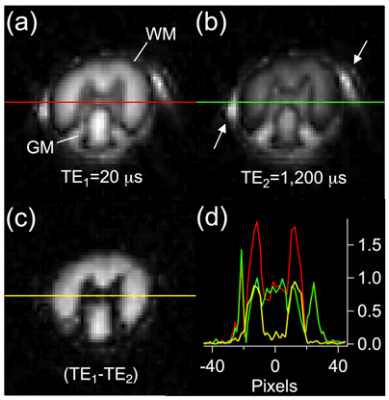

Fig. 2. The 3D de-IR-UTE images from rat thoracic SC averaged over five central slices. Magnitude images obtained for (*A*) TE = 20 μs, (*B*) TE = 1,200 μs, and (*C*) complex difference (*A* − *B*) (maximum-intensity range decreased by a factor of two to highlight myelin signal). (*D*) Intensity profiles across the three images (delineated as red, green, and yellow lines in *A*, *B*, and C, respectively) to show relative WM, GM, and background intensity. The most intense signal, present in the short- and long-echo profiles, originates from residual surface water. WM and GM are indicated in *A*, and arrows highlight residual surface water in *B*. The dark boundary observed at the GM/WM and WM/surface water interfaces in both echo images stems from partial voluming of adjacent regions with different T_1 resulting in destructive interference.

highlight the short T_2^* signal, which predominantly results from myelin protons.

MR Signal Dependence on Myelin Concentration. To separate the myelin and water peaks in the ^{1}H spectra of the myelin-D_2O suspensions, the spectra were modeled as a weighted sum of four super-Lorentzians (SL) for myelin resonances representing protons from general alkyl chain methylenes (noncholesterol, mostly from fatty acid residues), cholesterol alkyl chain methylenes, terminal methyls, and choline, and a Lorentzian for the HDO peak (details in *Materials and Methods*). Fig. 3*A* shows the results from fitting of the proton NMR spectrum of purified myelin suspended in D_2O. The fitting results were virtually identical for all myelin concentrations. Even though the signal envelope is very broad, relatively narrow resonances are also observed, likely due to proton pairs aligned with an average orientation at the magic angle relative to the static field (24).

Relative signal fractions, accounting for losses during excitation and acquisition, along with associated T_2^* distributions of the four SL components, were combined into a myelin T_2^* histogram (Fig. 3*B*). At 20 °C, 26.4% of the total signal has an effective lifetime of <25 μs, 51.8% of <100 μs, and 91.6% of <1,000 μs. At 37 °C these values are 16.9%, 44.8%, and 86.3%, respectively.

Fig. 4*A* shows a series of fitted myelin signals as a function of decreasing myelin concentration. The NMR signal areas for the total and separate spectral components (i.e., HDO and myelin) are plotted in Fig. 4*B*, indicating linear scaling with myelin concentration (R^2 = 0.99). We attribute the positive correlation of the water peak area with myelin concentration as resulting from labile protons from myelin constituents exchanging with D_2O to form HDO. The calculated average percentage of labile protons, for each of the 10 myelin lipid components, is listed in Table 1. The average signal contribution from the 0.1% impurity of the D_2O solvent, calculated as the y-intercept from the line of best fit (Fig. 4*B*), was subtracted from all of the HDO points, yielding an estimate of the labile myelin proton signal contribution. The predicted range of signal contributions from labile protons (5.05% ± 0.79%) agreed well with the experimental HDO peak areas (5.13% ± 2.00%). Given the excess D_2O used

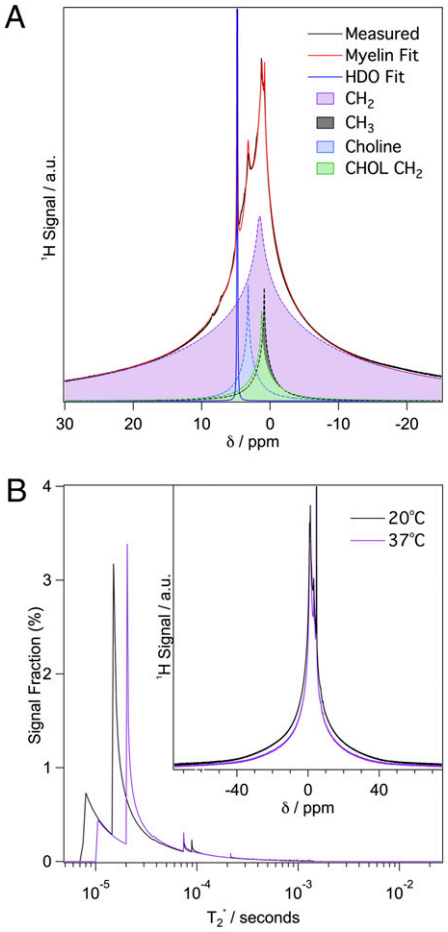

Fig. 3. ^{1}H NMR spectra and analysis of purified bovine myelin extract suspended in D_2O. (*A*) NMR spectrum (black) and SL fitting showing the resulting myelin (red) and HDO (blue) fits, as well as the four individual SL components of myelin (shaded). The four fitted SL components consisted of (*i*) SL containing 74.3% of the intensity, centered at 1.5 ppm, corresponding to the general alkyl chain methylene protons (CH_2), (*ii*) SL containing 12.4% of the intensity, centered at 0.9 ppm, corresponding to the terminal methyl protons (CH_3), (*iii*) SL containing 11.1% of the intensity, centered at 3.2 ppm, corresponding to the choline methyl protons (Choline), and (*iv*) SL containing 2.1% of the intensity, centered at 1.3 ppm, corresponding to the cholesterol alkyl chain methylene protons (CHOL CH_2). (*B*) T_2* histogram of myelin components at 20 and 37 °C derived from the SL fitting. There are small T_2* components that extend up to 26 ms, but these cannot be observed at the displayed scale. *Inset*: Myelin extract spectra collected at the two temperatures.

in the suspensions, it is reasonable to assume that all labile myelin protons had exchanged with deuterium.

Fig. 5 *Inset* shows the complex difference 2D projection de-IR-UTE image for a series of myelin suspensions of increasing concentration. Region of interest (ROI) average intensities from each of the myelin samples in the image are plotted in Fig. 5 and, analogous to the spectral data, are linearly correlated with myelin concentration (R^2 = 0.98).

On the basis of the relaxation characteristics of myelin (notably the lifetime of the various T_2^* components), Bloch equation simulations (details in *SI Materials and Methods*) accounting for losses sustained during the rf pulse sampling suggest that, under the spectral recording conditions, 81.7% of the total spectral signal is recovered, where the shorter T_2^* components account for the majority of the signal lost. The depletion of the imaging signal is more severe because it entails coherence losses during both

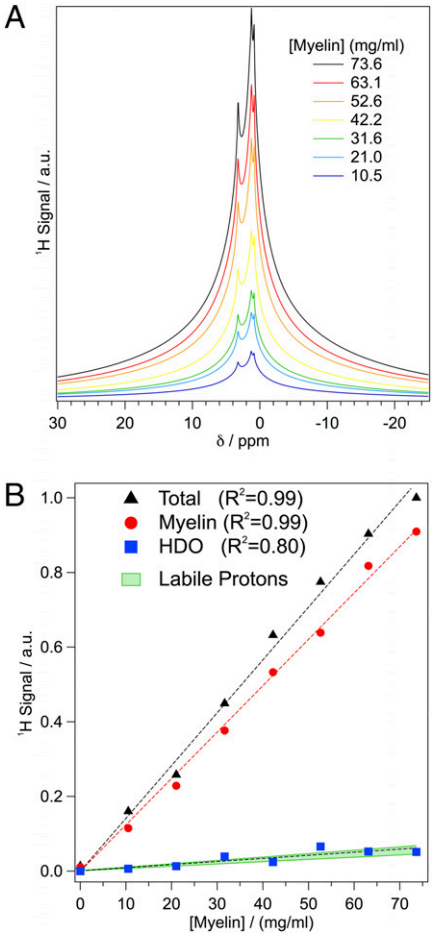

Fig. 4. (*A*) Fitted myelin peaks for myelin suspensions of various concentrations. (*B*) Linear correlation plot of MR signal as a function of myelin concentration for the total (triangle), myelin (circle), and HDO (square) signal components with calculated R^2 values. All two-tailed P values <0.01. Also shown is the calculated signal fraction of labile myelin protons (green shaded).

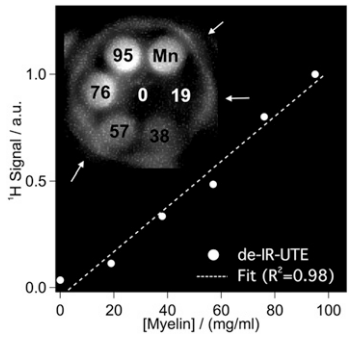

Fig. 5. UTE imaging and analysis of purified bovine myelin extract suspended in D_2O. *Inset*: The 2D projection de-IR-UTE image of six 5-mm NMR tubes filled with myelin/D_2O suspensions of varying concentrations (mg/mL). Mn indicates the tube containing manganese-doped water. Plot of the normalized de-IR-UTE mean ROI intensities vs. myelin concentration (P = 0.0002). Arrows indicate areas of signal from paper towel used to stabilize the tubes.

the adiabatic inversion and excitation pulses, as well as during the period preceding collection of the low-spatial frequencies (TE) and partial saturation. We estimate that with the imaging parameters used in our experiments, 38.0% of the total available myelin proton signal could be recovered.

Discussion

In this work we explored the feasibility of direct imaging and quantification of myelin by magnetic resonance as an alternative to indirect detection techniques such as MT or T_2 relaxometry. Direct detection of myelin would remove any ambiguities in analysis and provide a contrast specific to myelin concentration. To explore the feasibility of direct myelin imaging, we first investigated the origins of the short T_2^* signal in intact SC and myelin extracts. We then presented preliminary UTE with long T_2^* suppression images of myelin in WM.

The purity of our myelin extract was validated by 9.4 T high-resolution proton-decoupled ^{31}P (Fig. S2*A*) and ^{13}C (Fig. S2*B*) NMR, showing good agreement with previously determined molar ratios (25) (Table 1). The slight variations are reasonable given the differences in the anatomical origin of the sample (brain vs. SC) (26), inherent variability of the measurement (27), and the developmentally immature nature of the tissue examined (26). Our ^{13}C spectra also agreed well with Husted et al.'s reported proton-decoupled magic-angle spinning (MAS) ^{13}C NMR spectra of isolated human myelin (28). In that study a synthetic ^{13}C spectrum of myelin was generated as a weighted sum of individual lipid spectra, based upon the known ratios of the individual lipid components. The synthetic spectrum was found to be in good agreement with the observed MAS spectrum, which in turn closely matches our solution spectrum (Fig. S2*B*), except for the absence of signals assigned to protein resonances in the MAS spectrum.

Any conclusions from extracted or synthetically produced myelin beg the question whether the resulting material retains the biophysical properties of native myelin. It is known that in aqueous suspensions myelin lipids spontaneously self-assemble into bilayer structures (i.e., vesicles). In this enthalpy-driven process (29) the myelin lipid suspension regains a structural order reminiscent of physiological myelin minus the protein component.

The spectrum of the isolated, reconstituted myelin exhibited a very broad line with relatively narrow components centered ~3.5 ppm upfield from water, consistent with methylene protons of alkyl chains, the main constituent of myelin. Further, this spectrum bears a high degree of similarity with that of neural tissue, which supports the notion that, upon aqueous suspension of the extract, a bilayer structure analogous to that for native myelin is reconstituted. The SC spectrum is expected to contain nonmyelin contributions such as from proteins. The difference spectrum (Fig. S3) suggests the presence of motionally restricted membrane proteins, along with a small fraction of mobile (perhaps cytoplasmic) proteins yielding narrow resonances.

The myelin resonance is consistent with the SL lineshape of a dipolar-broadened liquid–crystalline lipid system (24, 30) as suggested by several lineshape properties (31), including a small second moment ($M_2 = 1.06 \times 10^8$ s^{-2}), a large fourth moment (M_4) to M_2 ratio [$M_4/(M_2)^2 = 6.57$], and a full width at 1/10 maximum ($\Delta\nu_{1/10}$) to full width at 1/2 maximum ($\Delta\nu_{1/2}$) ratio >3 ($\Delta\nu_{1/10}$: $\Delta\nu_{1/2} = 7$). Following previous work (32), we modeled the myelin lipid extract spectrum as a sum of SLs representing protons from general alkyl chain methylenes, cholesterol alkyl chain methylenes, terminal methyls, and choline. Although the T_2^* distribution showed a wide range of values (0.008–26 ms), the distribution was dominated by that of the alkyl chain methylenes because they make up ~75% of the four myelin lipid proton moieties under consideration. One notes a bimodal distribution (Fig. S5) with the first peak significantly attenuated as expected for an SL lineshape determined by the angular dependence of T_2^* (details in *SI Results*).

In contrast to the SL fitting performed in this work, Horch et al. performed multiexponential fitting of the time-domain signal decay (18). Although the SL lineshape theoretically

cannot be described with a basis set of exponential functions, the authors suggested that the resulting errors would be small for the case of myelin. Horch et al. analyzed free-induction decay signals of myelinated mammalian and amphibian nerves, as well as synthetic myelin at 4.7 T, yielding histograms of relaxation times. The authors detected significant components with T_2^* values of 20 and 70 μs in frog sciatic nerve, which they conjectured to arise from protein and methylene protons of myelin, respectively. In contrast, because our myelin extract was free of protein, the present data alternatively suggest the short T_2^* components (<25 μs) to arise from myelin lipids. This is not to imply that membrane proteins cannot contribute a short T_2^* component, as suggested by the broad resonance in the difference spectrum (Fig. S4) and in other reports (24, 33).

In bovine myelin suspended in D_2O, we found the integrated spectral areas to scale linearly with myelin concentration (Fig. 4), as did ROI intensities of the 2D projection de-IR-UTE images (Fig. 5), thus suggesting that quantitative myelin imaging may be feasible. Direct 3D de-IR-UTE imaging of a rat SC in situ at 400 MHz highlights the potential of such an approach, as demonstrated with images showing signal from the WM regions only. Absolute quantification would require a reference sample, ideally with relaxation and density properties matching myelin. The reference sample should also be chemically stable.

Previously, Waldman et al. (23) obtained images of the human brain using a slice-selective UTE along with soft-tissue suppression, essentially showing intense signal from WM regions of the brain, which they attributed to short T_2^* components. Under these conditions [i.e., selective half-*sinc* pulses of 400- to 600-μs duration (34)], all but the longest T_2^* components of the myelin protons would elude detection.

Our results indicate approximately 20% of the protons in myelin lipids to have an effective T_2^* less than 25 μs. Even under the more favorable conditions of our imaging experiments, the majority of these short T_2^* components remains undetectable. The very short lifetime of the signal has potentially adverse effects on the point-spread function (PSF) manifesting as blurring. A simple estimation based on the FWHM of the spectra (Fig. 3) predicts an intrinsic resolution (defined as the minimum achievable pixel size) on the order of 100 μm, which is approximately one pixel with our current imaging parameters (more details in *SI Materials and Methods*). It should be noted that although the blurring from the shortest T_2^* component would be greater, its impact on the PSF is negligible because this signal fraction remains virtually undetected.

A limitation that needs to be noted for this method is that it detects myelin solely on the basis of its T_2^* properties. Thus, errors in long T_2^* suppression may lead to signal misclassified as short T_2^* and hence falsely identified as myelin. Such errors could be accounted for and perhaps mitigated by tailoring a reference sample so as to contain water of comparable concentration and relaxation times to those of neural tissue. Last, there are other possible nonmyelin short T_2^* sources that could contribute to the UTE image intensity, including glial cell membranes, calcifications, tissue scars, vasculature, and hemorrhage (23), that would be indistinguishable from myelin.

Another potential problem could arise from saturation of the myelin signal via cross-relaxation (35). Even though adiabatic inversion of tissue water has minimal direct effect on the myelin lipid proton signal, transfer of magnetization from the water to the myelin proton pool could occur via chemical exchange or dipolar coupling. This mechanism would result in a reduction in the detected myelin signal, an effect that requires further scrutiny.

The potential for translation of the method to the clinic will be challenging. Nevertheless, it is encouraging to note that with dedicated hardware rf pulses of 20 μs or less have already been shown to be feasible on clinical equipment at 3 T field strength, as in recent work by Wu et al., who imaged the collagen matrix of cortical bone (36). Further, at 37 °C the measured T_2^* values increase by *ca.* 30% (Fig. 3*B*), raising the minimum T_2^* value from 8 to 10.5 μs. At body temperature the scan parameters used in our current experiments at 9.4 T (except for a 20-μs hard pulse of 7.6° flip angle to match the peak B_1 amplitudes of clinical head coils) predict 4.9% of the total myelin proton signal [i.e., 0.7% of the total proton signal given that myelin accounts for 14% of WM (1)] to be recoverable on a 3 T clinical MRI system (for calculation details see *SI Materials and Methods*).

Given that tissue proton concentration is ∼100 M, the concentration of detectable myelin protons is approximately 700 mM. In comparison with proton MR spectroscopic imaging (MRSI) of brain metabolites, where the metabolite concentrations are on the order of 10 mM, detectable myelin proton concentration, and hence intrinsic SNR, should be a factor of approximately 70 greater than that of typical metabolites. However, this gain in SNR compared with MRSI is mitigated by the reduced sampling time imposed by the much shorter T_2^* of the protons in myelin compared with those in brain metabolites. We estimate reduced overall sampling time to result in a loss on the order of a factor of 10. Given a reported resolution for MRSI of 5–10 mm (37), we project the resolution achievable with our method to be roughly on the order of 2.5–5 mm with T_2^*-induced PSF blurring not exceeding 0.6 mm (*SI Results*).

Conclusions

We have characterized the spectral properties of the myelin proton signal in situ, as well as in reconstituted suspensions of myelin lipid extract. Our results show that the short T_2^* component of WM originates primarily from myelin lipid protons and further that direct imaging of these protons is possible even though the shortest components are not detectable. Last, our analysis suggests that translation from the laboratory to clinical MRI will be challenging.

Materials and Methods

All MR spectroscopy and imaging experiments were performed on a 9.4 T vertical-bore spectrometer/microimaging system (Bruker DMX 400) with Micro2.5 gradients (100 G/cm maximum strength) and BAFPA40 amplifiers.

Neural Tissue Preparation. SC samples were harvested from healthy adult Sprague-Dawley rats (Charles River Laboratories) and bovine spinal columns (Bierig Brothers Veal and Lamb Products). The rats were killed by carbon dioxide asphyxiation in accordance with an Institutional Animal Care and Use Committee-approved protocol. After killing, rat spinal columns were removed, and the SC was dissected out.

NMR Spectroscopy. High-resolution proton-decoupled ^{13}C NMR [Sweep width (SW) = 24 kHz, number of scans (NS) = 36,768, number of real and imaginary data points (TD) = 65,536, repetition time (TR) = 1.36 s, α = 30°] and proton-decoupled ^{31}P (SW = 3.23 kHz, NS = 8,536, TD = 8,192, TR = 1.27 s, α = 30°) spectra were collected for samples of purified bovine myelin extract, dissolved in a (5:4:2) ternary mixture of deuterated chloroform (99.8 atom % D; Acros Organics), methanol (99.8 atom % D; Acros Organics), and 0.2 M EDTA/water (99.9 atom % D; Sigma-Aldrich).

All ^1H NMR spectra were collected with the following parameters: SW = 100 kHz, NS = 256, TD = 262,144, TR = 3.6 s, α = 90°, pulse duration = 9.6 μs. Freshly excised SC sections (<2-h postmortem interval) were immersed in a perfluorinated oil (Fomblin-Y; Sigma-Aldrich) before experiments.

SL Fitting of Proton Spectrum. As described by Wennerström (30), only partial averaging of dipolar coupling via translational and rotational diffusion occurs, resulting in a dipolar-broadened liquid–crystalline lipid system with an SL lineshape that can be written as:

$$L(\omega) = \int_0^{\pi/2} \frac{\sin(\theta)}{\left|3\cos^2(\theta)-1\right|} f\left[\frac{\omega-\omega_0}{\left|3\cos^2(\theta)-1\right|}\right] d\theta \qquad [1]$$

where ω_0 is the chemical shift, θ is the angle of the lipid bilayer surface normal with respect to B_0, and $f(\omega\text{-}\omega_0)$ is any highly peaked lineshape such as

a Gaussian or Lorentzian. Assuming θ is uniformly sampled and setting $f(\omega-\omega_0)$ to be a Lorentzian, it can be seen from Eq. **1** that an SL is composed of a series of scaled Lorentzians. From the widths and intensities of these Lorentzians, the T_2* distribution of a single SL can be calculated. Protons at different chemical shifts (e.g., alkyl chain methylenes, terminal methyls, and choline) are each expected to give rise to SL lineshapes (32).

Spectral fitting was performed in Matlab (Mathworks). Four SLs were used to represent general alkyl chain methylenes (noncholesterol, mostly from fatty acid residues), cholesterol alkyl chain methylenes, terminal methyls, and choline, whereas a single Lorentzian was used to model residual HDO. Because cholesterol alkyl chain methylenes sit deep within the lipid bilayer, it is reasonable to expect them to be more mobile than the general alkyl chain methylenes, therefore resulting in a narrower SL. The chemical shifts of each SL were set to the known isotropic shift of the various moieties, and the width and relative intensities were free parameters. The R^2 of the fit was greater than 0.99.

UTE MR Imaging. The 3D de-IR-UTE imaging (Fig. S4): SW = 200 kHz, TE = 20/1,200 μs, TI = 500 ms, TR = 1 s, field of view = 15 mm, matrix size = 128 × 128 × 128, number of views = 5,342, pulse duration = 20 μs. The sequence was based on that used by Anumula et al. (38). TI was determined empirically as the duration yielding optimal GM suppression (because GM is expected to have negligible myelin concentration) in a complex difference image. A refocusing gradient was applied immediately after the first readout gradient, after which a second gradient echo was collected at TE = 1,200 μs. A 3D image of the short T_2* components was obtained as the complex difference of the two echo images (i.e., $TE_1 - TE_2$). A complex difference is necessary to distinguish the possible presence of both inverted and non-inverted voxel signals.

A 2D projection de-IR-UTE sequence was used to image the series of myelin/D_2O suspensions to avoid signal losses resulting from settling of myelin during scanning. The Mn doped water phantom served to identify the locations of the samples in the image. All experimental parameters were identical to those used in the 3D de-IR-UTE experiments.

All image reconstruction was done in Matlab (Mathworks) using a fast gridding algorithm (39) and incorporating k-space trajectory correction (40). All images were smoothed via bilinear interpolation with Image J (National Institutes of Health).

ACKNOWLEDGMENTS. We thank Joseph J. Sarver and Louis J. Soslowsky for providing a source of fresh rat CNS tissue and Jim Delikatny and Jeremy Magland for their help with the super-Lorentzian analysis. M.J.W. thanks Mary A. Selak for patient guidance and assistance perfecting the sucrose gradient-based isolation of myelin. This work was supported by National Institutes of Health Grant T32 EB00814 and US Department of Defense Award W81XWH-10-1-0714.

1. van der Knaap MS, Valk J (2005) *Magnetic Resonance of Myelination and Myelin Disorders*, eds Heilmann U, Mennecke-Buhler D (Springer, Berlin), pp 1–19.
2. Káradóttir R, Hamilton NB, Bakiri Y, Attwell D (2008) Spiking and nonspiking classes of oligodendrocyte precursor glia in CNS white matter. *Nat Neurosci* 11:450–456.
3. Laule C, et al. (2006) Myelin water imaging in multiple sclerosis: Quantitative correlations with histopathology. *Mult Scler* 12:747–753.
4. Avila RL, et al. (2005) Structure and stability of internodal myelin in mouse models of hereditary neuropathy. *J Neuropathol Exp Neurol* 64:976–990.
5. Wang H, Fu Y, Zickmund P, Shi R, Cheng JX (2005) Coherent anti-stokes Raman scattering imaging of axonal myelin in live spinal tissues. *Biophys J* 89:581–591.
6. Fu Y, Huff TB, Wang HW, Wang H, Cheng JX (2008) Ex vivo and in vivo imaging of myelin fibers in mouse brain by coherent anti-Stokes Raman scattering microscopy. *Opt Express* 16:19396–19409.
7. Frullano L, Wang C, Miller RH, Wang Y (2011) A myelin-specific contrast agent for magnetic resonance imaging of myelination. *J Am Chem Soc* 133:1611–1613.
8. Stankoff B, et al. (2006) Imaging of CNS myelin by positron-emission tomography. *Proc Natl Acad Sci USA* 103:9304–9309.
9. Dousset V, et al. (1992) Experimental allergic encephalomyelitis and multiple sclerosis: Lesion characterization with magnetization transfer imaging. *Radiology* 182:483–491.
10. Mottershead JP, et al. (2003) High field MRI correlates of myelin content and axonal density in multiple sclerosis—a post-mortem study of the spinal cord. *J Neurol* 250: 1293–1301.
11. Whittall K, Mackay A (1989) Quantitative interpretation of NMR relaxation data. *Magn Reson Med* 84:134–152.
12. MacKay A, et al. (1994) In vivo visualization of myelin water in brain by magnetic resonance. *Magn Reson Med* 31:673–677.
13. Gulani V, Webb AG, Duncan ID, Lauterbur PC (2001) Apparent diffusion tensor measurements in myelin-deficient rat spinal cords. *Magn Reson Med* 45:191–195.
14. Laule C, et al. (2008) Myelin water imaging of multiple sclerosis at 7 T: Correlations with histopathology. *Neuroimage* 40:1575–1580.
15. Schmierer K, Scaravilli F, Altmann DR, Barker GJ, Miller DH (2004) Magnetization transfer ratio and myelin in postmortem multiple sclerosis brain. *Ann Neurol* 56: 407–415.
16. Lecar H, Ehrenstein G, Stillman I (1971) Detection of molecular motion in lyophilized myelin by nuclear magnetic resonance. *Biophys J* 11:140–145.
17. Ramani A, Aliev AE, Barker GJ, Tofts PS (2003) Another approach to protons with constricted mobility in white matter: Pilot studies using wideline and high-resolution NMR spectroscopy. *Magn Reson Imaging* 21:1039–1043.
18. Horch RA, Gore JC, Does MD (2011) Origins of the ultrashort-T2 1H NMR signals in myelinated nerve: A direct measure of myelin content? *Magn Reson Med* 66:24–31.
19. Wu Y, et al. (1998) Evaluation of bone mineral density using three-dimensional solid state phosphorus-31 NMR projection imaging. *Calcif Tissue Int* 62:512–518.
20. Robson MD, Gatehouse PD, Bydder M, Bydder GM (2003) Magnetic resonance: An introduction to ultrashort TE (UTE) imaging. *J Comput Assist Tomogr* 27:825–846.
21. Techawiboonwong A, Song HK, Wehrli FW (2008) In vivo MRI of submillisecond T(2) species with two-dimensional and three-dimensional radial sequences and applications to the measurement of cortical bone water. *NMR Biomed* 21:59–70.
22. Wu Y, et al. (1999) Multinuclear solid-state three-dimensional MRI of bone and synthetic calcium phosphates. *Proc Natl Acad Sci USA* 96:1574–1578.
23. Waldman A, et al. (2003) MRI of the brain with ultra-short echo-time pulse sequences. *Neuroradiology* 45:887–892.
24. Bloom M, Holmes K, Mountford C, Williams P (1986) Complete proton magnetic resonance in whole cells. *J Magn Reson* 69:73–91.
25. Norton WT, Autilio LA (1966) The lipid composition of purified bovine brain myelin. *J Neurochem* 13:213–222.
26. Norton WT (1974) Isolation of myelin from nerve tissue. *Methods Enzymol* 31(Pt A): 435–444.
27. Norton WT, Autilio LA (1965) The chemical composition of bovine CNS myelin. *Ann N Y Acad Sci* 122:77–85.
28. Husted C, Montez B, Le C, Moscarello MA, Oldfield E (1993) Carbon-13 "magic-angle" sample-spinning nuclear magnetic resonance studies of human myelin, and model membrane systems. *Magn Reson Med* 29:168–178.
29. Wimley WC, White SH (1993) Membrane partitioning: Distinguishing bilayer effects from the hydrophobic effect. *Biochemistry* 32:6307–6312.
30. Wennerström H (1973) Proton nuclear magnetic resonance lineshapes in lamellar liquid crystals. *Chem Phys Lett* 18:41–44.
31. MacKay AL (1981) A proton NMR moment study of the gel and liquid-crystalline phases of dipalmitoyl phosphatidylcholine. *Biophys J* 35:301–313.
32. Ulmius J, Wennerström H, Lindblom G, Arvidson G (1975) Proton NMR bandshape studies of lamellar liquid crystals and gel phases containing lecithins and cholesterol. *Biochim Biophys Acta* 389:197–202.
33. MacKay AL, Burnell EE, Bienvenue A, Devaux PF, Bloom M (1983) Flexibility of membrane proteins by broad-line proton magnetic resonance. *Biochim Biophys Acta* 728:460–462.
34. Sussman MS, Pauly JM, Wright GA (1998) Design of practical T2-selective RF excitation (TELEX) pulses. *Magn Reson Med* 40:890–899.
35. Edzes HT, Samulski ET (1977) Cross relaxation and spin diffusion in the proton NMR or hydrated collagen. *Nature* 265:521–523.
36. Wu Y, et al. (2010) Bone matrix imaged in vivo by water- and fat-suppressed proton projection MRI (WASPI) of animal and human subjects. *J Magn Reson Imaging* 31: 954–963.
37. Gruber S, Mlynárik V, Moser E (2003) High-resolution 3D proton spectroscopic imaging of the human brain at 3 T: SNR issues and application for anatomy-matched voxel sizes. *Magn Reson Med* 49:299–306.
38. Anumula S, et al. (2006) Measurement of phosphorus content in normal and osteomalacic rabbit bone by solid-state 3D radial imaging. *Magn Reson Med* 56:946–952.
39. Greengard L, Lee JY (2004) Accelerating the nonuniform fast fourier transform. *SIAM Rev* 46:443–454.
40. Rad HS, et al. (2011) Quantifying cortical bone water in vivo by three-dimensional ultra-short echo-time MRI. *NMR Biomed* 24:855–864.

5513

Prospects for quantitative imaging of myelin with dual-echo short inversion time 3D UTE MRI

M. J. Wilhelm[1], H. H. Ong[1], S. L. Wehrli[2], P-H. Tsai[1], D. B. Hackney[3], and F. W. Wehrli[1]

[1]Laboratory for Structural NMR Imaging, Department of Radiology, University of Pennsylvania, Philadelphia, PA, United States, [2]NMR Core Facility, Children's Hospital of Philadelphia, Philadelphia, PA, United States, [3]Department of Radiology and Neurology, Harvard Medical School, Beth Israel Deaconess Medical Center, Boston, MA, United States

Introduction

Myelin is a lipid bilayer sheath encasing axons that enhances nerve conduction efficiency. Malformation or loss of myelin is at the core of many neurodegenerative disorders[1]. At present, there are few alternatives to destructive histologic methods to directly assess myelin. While MRI relaxometry and diffusion methods can indirectly assess myelin, they only detect myelin-associated water and not myelin itself. The short T_2^* of myelin protons and the presence of strong long T_2^* signals in white matter (WM) have thus far prevented direct myelin imaging with MRI. In this work, we examine the feasibility of ultra-short echo time (UTE) MRI to directly image myelin in purified myelin extracts and excised rat spinal cords (SC). NMR is first used to identify and characterize the MR signal from myelin. A dual-echo short inversion-time UTE sequence (de-STUTE) based on Ref. 2 is then used to suppress the long T_2^* signal and image a rat SC.

Methods

Rat and bovine SC samples were harvested from Sprague-Dawley rats (Charles River Labs) and a local butcher. A sucrose gradient method[3] was used to extract myelin from SC tissue using both WM and grey matter (GM). This method has been shown to preserve the bilayer structure of myelin. The myelin extract was suspended in D_2O (99.9% D, Sigma-Aldrich). Bovine myelin extract was used to prepare myelin/D_2O mixtures with varying myelin concentration (1.24-17.36 mg/ml). All spectroscopic and imaging experiments were performed on a 9.4 T vertical bore spectrometer/micro-imaging system (DMX-400, Bruker Instruments).

^{1}H NMR spectra were obtained for a freshly excised rat thoracic SC immersed in Fomblin (Sigma-Aldrich), as well as bovine and rat myelin extracts and samples with varying myelin concentration. Rat and bovine myelin extract was also dissolved in an organic solvent mixture to acquire high-resolution ^{1}H, and ^{31}P and ^{13}C proton-decoupled NMR spectra for identification of lipid components.

The rat thoracic SC section was imaged using a 2D de-STUTE sequence (128x128, FOV ~2cm). A 5ms adiabatic inversion pulse and 500ms inversion time were used to selectively invert and null long T_2^* signal. A 2D ramp-sampled UTE image with hard pulse excitation was then acquired with TE=10μs. Following a refocusing gradient, another 2D UTE image was acquired with TE=1200μs. A magnitude subtraction of the long TE image from the short TE image suppressed any residual long T_2^* signal.

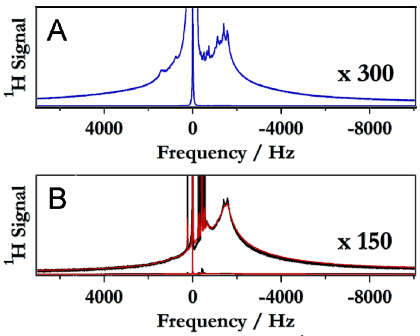

Fig 1. Full-scale and magnified ^{1}H spectra of intact rat SC (A) and myelin extract (B) for rat (red) and bovine (black). Spectra centered on water frequency. Note intact SC needed higher magnification to see broad peak.

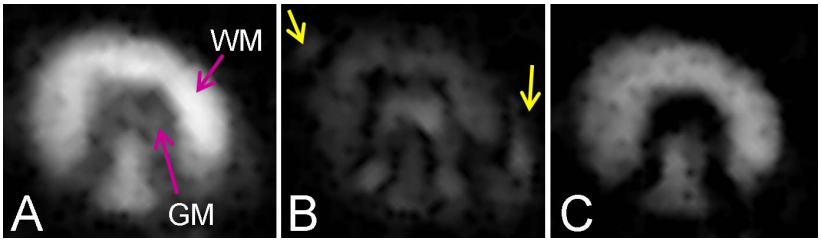

Fig 2. Linearly interpolated 2D de-STUTE images of excised rat thoracic SC section. A) TE=10μs. GM and WM are as indicated. B) TE=1200μs. Yellow arrows show residual surface water. C) Magnitude difference image of B from A.

Results and Discussion

Fig. 1 shows ^{1}H NMR spectra for intact rat SC and rat/bovine myelin extracts. The intact rat SC spectrum highlights the dominant water peak that would mask any myelin signal without long T_2^* suppression. The myelin extract spectra show residual sucrose and water peaks. The water peak is reduced as the myelin extract is mixed in D_2O. All three spectra share a non-Lorentzian, broad resonance (linewidth ~1700Hz) whose center is shifted ~3.5 ppm upfield from the water peak, which is consistent with the chemical shift of methylene protons in lipids. High-resolution ^{1}H, ^{31}P and ^{13}C spectra of myelin extract (not shown) are consistent with the galactolipid, phospholipid, and cholesterol constituents of myelin[4] and show negligible contributions from proteins. This strongly supports that the short T_2^* signal of SC consists predominantly of myelin lipids.

From its line width, T_2^* of myelin was estimated to be 100-200μs. Therefore, ramp-sampled UTE MRI should detect this signal with TE=10μs. Figure 2 shows de-STUTE images from a rat thoracic SC section. The short TE image shows good contrast between WM and GM. The long TE images shows a significant decrease in overall signal intensity implying that the short TE image contains a substantial amount of short T_2^* signal. The dark boundary between GM/WM and SC/water is the result of partial volume averaging of adjacent regions with different T_1s leading to destructive interference near the null time. The magnitude difference shows excellent suppression of GM and residual water outside the SC. The short T_2^* signal resides entirely in WM, which suggests that myelin is being imaged. Figure 3 shows ^{1}H spectra of various concentrations of myelin extract. The peak integrals are highly correlated with myelin extract concentration. The data highlight the potential of de-STUTE to quantify myelin concentration using a reference. Further work is needed to develop a 3D de-STUTE sequence and construct a reference phantom with similar relaxation properties to myelin analogous to the approach in Ref. 5.

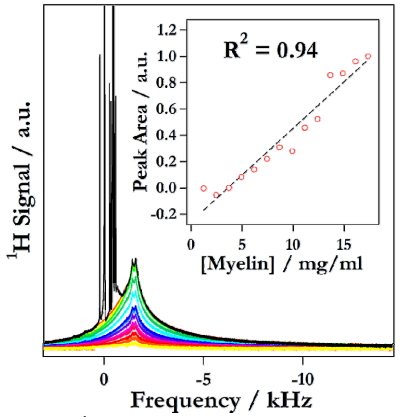

Fig 3. ^{1}H spectra for a series of bovine myelin extract concentrations. Residual sucrose and water peaks (black) were removed using a bi-exponential fit of the broad peak. Inset: Fitted broad peak area vs myelin concentration.

Conclusion

This work examined the potential for de-STUTE to directly image and quantify myelin. NMR results indicates that the short T_2^* signal of SC is predominantly myelin lipids. de-STUTE images exhibit a short T_2^* signal present only in WM, which suggests the constituent imaged is indeed myelin.

References: 1. van der Knaap, MS et al, *Magnetic Resonance of Myelin, Myelination, and Myelin Disorders*, Springer-Verlag (1995). 2. Waldman, A et al, *Neuroradiology*, **45**:887 (2003). 3. Larocca, JN et al, *Curr. Protoc. Cell Biol.*, 3.25.1 (2006). 4. Husted, C et al, *MRM*, **29**:168 (1993). 5. Techawiboonwong, A et al, *Radiology*, **248**:824 (2008). **Acknowledgements:** NIH T32 EB00814

Feasibility of low q-space diffusion MRI at 1.5T

Henry H. Ong[1], Yusuf Bhagat[1], Jeremy Magland[1], and Felix W. Wehrli[1]
[1]*Laboratory for Structural NMR Imaging, Departement of Radiology, University of Pennsylvania School of Medicine, Philadelphia, PA, United States*

Introduction

By exploiting the regularity of molecular diffusion restrictions such as axon membranes and myelin sheaths[1], q-space imaging[2,3] (QSI) offers potential for indirect assessment of white matter (WM) axonal architecture. For example, QSI can accurately estimate mean axon diameter (MAD) and intracellular volume fraction (ICF)[4,5]. Unfortunately, the application of QSI on a clinical scanner is severely constrained by the low gradient strengths available, which limits the maximum achievable q-value ($q = (2\pi)^{-1}\gamma G\delta$, G = gradient amplitude, and δ = gradient duration). Low maximum q-value leads to insufficient displacement resolution to accurately study axons, which have an MAD of 1-3 µm. Low q-value diffusion MRI[5], in which axonal architecture information is extracted by fitting the q-space signal decay (E(q)) at low q-values ($q^{-1} >>$ MAD) under the short gradient pulse approximation (SGPA), does not require high gradient amplitudes. However, low clinical gradient strengths lead to violation of SGPA. Here, we test the feasibility of implementing low q-value diffusion MRI on a 1.5T system by assessing axonal architecture in excised fixed pig spinal cords.

Methods

As described in [5], at low q-values ($q^{-1} >>$ MAD), the signal decay is given by $E(q)=\exp(-2\pi^2q^2Z^2)$ (Eq.1), where Z is the root mean squared (RMS) displacement of diffusing molecules during a diffusion time Δ[6,7]. As E(q) contains signal from extra- and intra-cellular spaces (ECS and ICS), a two-compartment version of Eq.1 can be defined: $E(q)= f_E\cdot\exp(-2\pi^2q^2Z_E^2) + f_I\cdot\exp(-2\pi^2q^2Z_I^2)$ (Eq. 2), where f_E and f_I are the relaxation-weighted ECS and ICS volume fractions and Z_E and Z_I are the RMS displacement of diffusing molecules in the ECS and ICS. From Eq. 2, MAD and ICF can be estimated from Z_I and f_I, respectively.

For validation of this method, five fixed cervical spinal cords (SC) harvested from five skeletally mature Yucatan mini-pigs were used. Before experiments, the SCs were placed in tubes filled with Fomblin (Sigma-Aldrich) to keep the specimens hydrated and to remove any background signal. The low q-value diffusion MRI method was implemented on a 1.5T Siemens Sonata MRI scanner (Erlangen, Germany) with 40 mT/m gradients using a custom single-slice PGSE with multi-shot fly-back EPI readout pulse sequence. The body coil was used for transmit and a custom-built 4-channel phased array coil (Insight MRI) was used for receive. The imaging parameters were: Δ/δ/TE = 98.7/55/257ms, 128×128, FOV = 64×64 mm, slice thickness = 10 mm, number of shots = 8, NA = 36, and TR = 2 s. The diffusion gradient was applied perpendicular to the SCs in 32 increments (q_{max} = 0.08 µm^{-1}) and the scan time ~5 hours. Note that these values for δ and Δ violate SGPA. All five SCs were imaged simultaneously. After Fourier transform, a 3D matrix of 32 2D images at various q-values was obtained. An average E(q) was measured in ROIs within the dorsal, ventral, and lateral columns of the SCs (Fig. 1). This average E(q) was fit with Eq. 2 under the constraint $f_E+f_I=1$.

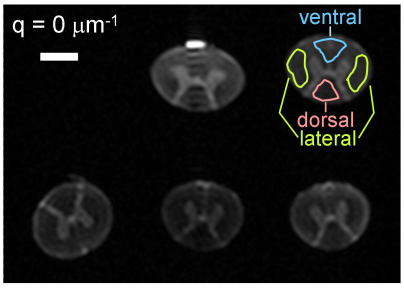

Fig. 1. Sample image at q = 0 µm^{-1}. White bar = 5 mm. ROI locations are shown for the dorsal, ventral and lateral WM columns. The bright spot above the center top SC is residual surface PBS.

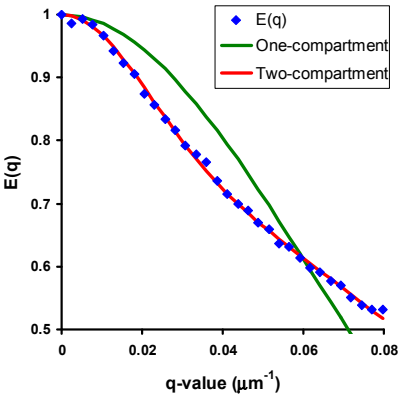

Fig. 2. Sample $E(q)$ for a lateral WM column ROI (blue diamonds) with one-compartment (green line) and two-compartment (red line) fits.

Results and Discussion

Fig. 2 shows a sample E(q) with the fit from Eq. 2. The fit shows good agreement with E(q) (R^2 >0.98). For display purposes, a one-compartment fit (Eq.1) is also shown to illustrate its poor agreement. Fig. 3 shows bar graphs of f_E, Z_E, f_I, and Z_I fitting results for each ROI averaged over all five SCs. Z_I falls within 1-2µm, which is the expected range of axon diameters in mammals[8]. Z_E is lower than that expected for free water (~20µm for Δ = 98.7ms). The ADC calculated from Z_E (~0.25×10^{-3} mm^2/s) agrees with literature values for fixed spinal cord WM tissue[9], which provides further evidence that ADCs measured at low b-values (<2500 s/mm^2) primarily reflect diffusion in ECS[10]. The average f_I was ~0.7, which falls within the expected ICF for WM[11]. An ANOVA analysis indicated no significant differences in f_I among the WM columns as previously seen in mouse SP[5]. Paired t-tests indicated that the dorsal column Z_E and Z_I are significantly smaller than those of the ventral WM column, which matches previous observations of smaller MAD and increased axon density in the dorsal compared with ventral columns[4,8,9].

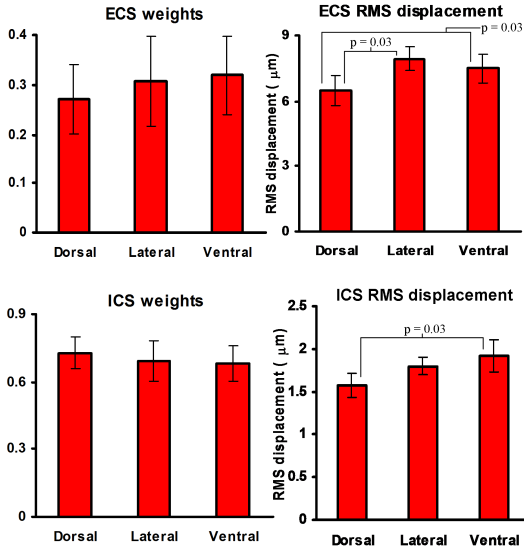

Fig. 3. Bar graphs of f_E (ECS weighting), Z_E (ECS RMS displacement), f_I (ICS weighting), and Z_I (ICS RMS displacement) fitting results Standard deviation bars are shown. Significant p-values (<0.05) of paired t-tests between the different ROIs are shown.

Conclusion

This work demonstrates the feasibility of implementing low q-value diffusion MRI on a 1.5T scanner. The results show that despite violating SGPA, this method has the potential to accurately assess regional axonal architecture with metrics such as MAD and ICF.

References: 1. Beaulieu, C, *NMR Biomed*, **15**:435 (2002). 2. Callaghan, PT, *Principles of NMR Microscopy*, Oxford University Press (1991). 3. Cohen, Y, *et al.*, *NMR Biomed*, **15**:516 (2002). 4. Ong, HH, *Neuroimage*, **40**:1619 (2008).. 5. Ong, HH, *Neuroimage*, **51**:1360 (2010). 6. Price W, *Concepts Magn Res*, **10**:299 (1997). 7. Kimmich R, *NMR: Tomography, Diffusometry, Relaxometry*, Springer-Verlag (1997). 8. Williams, PL, *et al.*, *Gray's anatomy*, Churchill Livingstone (1995). 9. Schwartz, ED, *et al.*, *AJNR*, **26**:390 (2005). 10. Schwartz, E.D., *et al.*, *Neuroreport*, **16**:73 (2005). 11. Sykova, E, *et al.*, *Physiol Rev*, **88**:1277 (2008). **Acknowledgements:** NIH R21 EB003951

Super-Lorentzian framework for investigation of T_2^* distribution in myelin

Michael J. Wilhelm[1], Henry H. Ong[2], and Felix W. Wehrli[2]

[1]*Department of Chemistry, Temple University, Philadelphia, PA, United States,* [2]*Laboratory for Structural NMR Imaging, Department of Radiology, University of Pennsylvania School of Medicine, Philadelphia, PA, United States*

Introduction

Deficiencies of myelin, a lipid bilayer sheath critical for normal function of white matter (WM), lay at the core of numerous neurodegenerative disorders such as multiple sclerosis and schizophrenia (1). At present, there are few alternatives to destructive histologic methods to directly assess myelin. The short T_2^* of myelin protons make ultra-short echo time (UTE) MRI a potential imaging modality to directly detect myelin (2). In contrast, indirect MRI methods such as magnetization transfer and T_2 relaxometry are based on complex interactions between water and myelin, which can lead to ambiguities in data analysis. Characterizing the T_2^* distribution of myelin is key to developing optimal UTE methods for myelin imaging. Previous attempts have used multi-exponential fitting of the FID (3), which is not only an ill-posed problem (4), but also theoretically incorrect. Myelin is a liquid crystalline lipid system that is described by a sum of super-Lorentzians (SL) rather than a multi-Lorentzian lineshape (5, 6). Here, we use this SL framework to calculate T_2^* distributions by fitting ^{1}H NMR spectra of myelin lipid extract and intact rat spinal cord (SC).

Theory and Methods

According to Wennerström (6), due to averaging effects from translational and rotational diffusion, for a given orientation of a lipid bilayer, the lineshape can be expressed as: $L(\delta\text{-}\delta_0, \theta) = |3\cos^2\theta - 1|^{-1} f[(\delta\text{-}\delta_0)/|3\cos^2\theta - 1|]$ (Eq.1), where δ is the chemical shift centered at δ_0, θ is the angle of the lipid bilayer surface normal with B_0, and $f(x)$ is any highly peaked lineshape such as a Gaussian or Lorentzian. The SL lineshape, $L_{SL}(\delta\text{-}\delta_0)$, results from a uniform sampling of θ from 0 to $\pi/2$: $L_{SL}(\delta\text{-}\delta_0) = \int L(\delta\text{-}\delta_0, \theta)\sin\theta\, d\theta$ (Eq.2). By assuming $f(x)$ to be a Lorentzian, it can be seen from Eqs. 1 and 2 that a SL is composed of a series of scaled Lorentzians. From the widths and intensities of these Lorentzians, the T_2^* distribution of a single SL can be calculated. Multiple SLs have been used to fit NMR spectra of model membrane systems in which the SLs arise from protons at different chemical shifts, e.g. alkyl methylenes, terminal methyls, and choline (7). Therefore, it is possible in theory to perform a multi-SL fit of a ^{1}H NMR spectrum of myelin and calculate a T_2^* distribution.

Rat and bovine SC samples were harvested from Sprague-Dawley rats (Charles River Labs) and a local butcher. Myelin lipids were extracted from bovine SC tissue with a sucrose gradient method (8), dissolution in a ternary mixture (chloroform/methanol/water), and lyophilization. Previous work has shown that this protocol extracts myelin lipids with little to no protein (2). Dehydrated myelin lipid extract was then re-suspended in 99.9% D_2O (Sigma-Aldrich) to regenerate a bilayer structure. ^{1}H NMR spectra at 9.4T (DMX-400, Bruker Instruments) were obtained for a freshly excised rat thoracic SC immersed in Fomblin (Sigma-Aldrich), as well as the myelin lipid extract. Rat SC was immersed in D_2O for 24 hrs prior to experiments to reduce the dominant tissue water peak.

Spectral fitting was performed in Matlab (Mathworks). Four SLs were used to represent general alkyl chain methylenes, cholesterol alkyl chain methylenes (as they have shorter chain lengths), terminal methyls, and choline, while a single Lorentzian was used to model residual HDO. The chemical shifts of each SL were set to the known isotropic shift of the various moieties, and the width and relative intensities were free parameters.

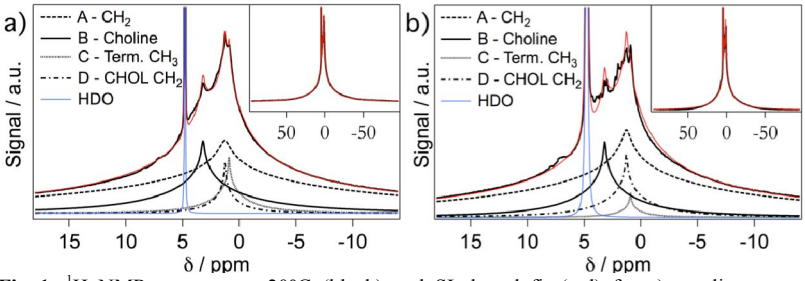

Fig 1. ^{1}H NMR spectra at ~20°C (black) and SL based fit (red) for a) myelin extract (R^2=0.999) and b) rat SC (R^2=0.997). The four SL and Lorentzian peaks of the fit are shown. Full spectral width is shown in inset with HDO peak truncated.

Results and Discussion

Fig. 1 shows myelin lipid extract and rat SC ^{1}H NMR spectra with the results of the four-component SL fits. Both spectra are comprised of a narrow peak from residual HDO and a broad resonance (linewidth ca. 1700Hz) from myelin. A large 4th to 2nd moment ratio (ca. 6.6), suggests that this broad resonance has a SL lineshape. The SC ^{1}H NMR spectrum had additional minor peaks from intracellular proteins and other non-myelin protons. Despite the additional complexity of the SC spectrum, both SL fits agree well with the ^{1}H NMR spectra ($R^2 > 0.99$). Fig. 2 shows the relative fractions (theoretical and fitted) of the four SL myelin components in myelin extract and intact rat SC. As expected, the signal is dominated (>70%) by alkyl methylene protons. Deviations from theoretical values may result from inaccuracies of the SL framework to describe non-chain alkyl protons, e.g. choline and terminal methyls.

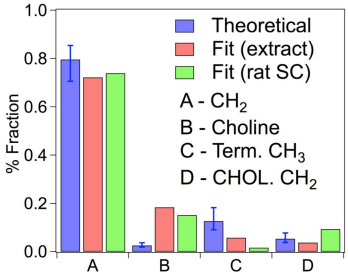

Fig 2. Relative fraction fitting results of the four SL components with expected theoretical fractions. Error bars account for variation in alkyl chain length.

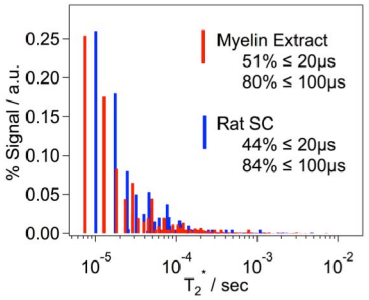

Fig 3. Calculated T_2* distributions for myelin lipid extract (red) and rat SC (blue). Signal fractions with T_2^* <20 and <100 μs are reported.

Fig. 3 shows the T_2^* distributions derived from the SL fits for the myelin lipid extract and SC. The T_2^* distributions are highly skewed with a wide range (10μs to 10ms). Despite this range, roughly 50% (80%) of the signal has a T_2^* less than 20μs (100μs). This result highlights the difficulty of direct myelin imaging even with UTE MRI. Further investigation is needed to study the system at body temperature as increased molecular motion is likely to result in longer effective T_2^*s.

Conclusion

This work uses a SL framework to characterize the T_2^* distribution of myelin, which would provide guidance toward developing UTE methods for myelin imaging. The results indicate that at ambient temperature ~50% of the myelin lipid proton signal has $T_2^* < 20$ μs.

References: 1. van der Knaap, MS et al, *Magnetic Resonance of Myelin, Myelination, and Myelin Disorders*, Springer-Verlag (1995). 2. Wilhelm, MJ et al, *Proc. of the ISMRM* (2011). 3. Horch et al, *Mag. Res. Med.*, **66**:24 (2011). 4. Epstein, CL et al, *SIAM Rev.*, **50**:504 (2008). 5. Bloom, M et al, *Chem. Phys. Lipids*, **4**:107 (1975). 6. Wennerstroem, H et al, *Chem. Phys. Lett.*, **18**:41 (1973). 7. Ulmius, J et al, *Biochim. Biophys Acta*, **389**:197 (1975). 8. Larocca, JN et al, *Curr. Protoc. Cell Biol.*, **3.25**:1 (2006). **Acknowledgements:** NIH T32 EB00814